VTT Technical Research Centre of Finland

3-D printed meat alternatives based on pea and single cell proteins and hydrocolloids: effect of paste formulation on process-induced fibre alignment and structural and textural properties

Calton, Alex; Lille, Martina; Sozer, Nesli

[Link to publication](#)

3-D printed meat alternatives based on pea and single cell proteins and hydrocolloids: Effect of paste formulation on process-induced fibre alignment and structural and textural properties

Alex Calton [*], Martina Lille, Nesli Sozer

VTT Technical Research Centre of Finland, Ltd., P.O. Box 1000, FI-02044 VTT, Finland

ARTICLE INFO

ABSTRACT

Extrusion-based 3D food printing can be used as an alternative structuring technique to traditional extrusion processing for creating meat-like structures. This study focused on 3-D food printing to generate structures analogous to meat by using various combinations of texturized pea protein fibrils, microbial Single Cell Protein (SCP) and hydrocolloids locust bean gum and/or sodium alginate. Simple moulding was utilized as benchmarking to better understand the 3D printing-induced structural effects. To gain understanding of the interactions between proteins of different origin (plant and SCP) and with hydrocolloids, structural, textural and rheological properties were analysed. Oscillatory stress sweeps of all printing pastes revealed elastic-dominant rheological behaviour (G' 4000–6000 Pa) with a defined yield stress (25–60 Pa) explaining their printability and shape stability. X-ray microtomography of ion-crosslinked analogues showed a printing-induced preferential alignment of fibrils in the direction of nozzle movement, while moulding led to a random orientation. Textural characterization via bi-directional cutting tests demonstrated higher cutting force in transversal (F_T) over longitudinal (F_L) direction in 3D-printed samples and equal forces in moulded samples. The anisotropy index ($AI = F_T/F_L$) of printed samples ranged between 1.4 and 2.5, indicating anisotropic texture, and 0.8–1 for moulded samples indicating isotropic texture. This study demonstrated the applicability of paste-extrusion in generating anisotropic structures analogous to meat by process-induced fibril alignment. The results support further development of 3D food printing technology in design of sustainable meat alternatives resembling whole-muscle meat.

1. Introduction

There is an increasing demand for sustainable alternatives to meat, which is driven by ethical, health and environmental concerns associated with animal meat consumption (Cornet et al., 2022). Increasing the proportion of plant-based over animal-based protein in the diet has been proposed to address these concerns (Willett et al., 2019). In addition, single cell protein (SCP), collectively known as the protein-rich biomass from algal, fungal or bacterial cells has been suggested as a viable alternative to feed a growing population since the 1960s (Ritala, Häkkinen, Toivari, & Wiebe, 2017). Recently, SCP production utilising direct air capture of CO_2 and hydrogen-oxidising bacteria in a closed system powered by renewable electricity was shown to require considerably less water and land compared to traditional protein sources

(Sillman et al., 2019). Bacterial SCP produced by gas fermentation can provide a high protein content (>65%), complete amino acid profile as well as bioactive compounds, such as B-group vitamins (riboflavin, niacin, choline, folic acid, cobalamine), minerals (iron and magnesium) and essential fatty acids (Ercili-Cura, Hakamies, Sinisalo, Vainikka, & Pitkanen, 2020). Fibrous, meat-like structures can be produced by thermo-extrusion using plant protein isolates or concentrates (Dekkers, Boom, & van der Goot, 2018). Low moisture (<30% moisture) extrusion tends to produce dry, spongy texturized vegetable protein (TVP), while a higher moisture content (>50%) produces non-expanded, fibrous gels when a long cooling die is included (Caporgno et al., 2020). Thermo-mechanical structuring processes are sufficiently scalable and resource efficient, but the produced structures are limited to various strips and chunks, or further reconstructed into comminuted products, such as

---

patties, which have randomly oriented fibres (Herz et al., 2021). Similarly, filamentous SCP, such as mycoprotein from *Fusarium venetatum*, rely on a freeze-texturization process, where aligned ice crystals drive filaments together to give meat-like texture in various shaped pieces (Miri, Barigou, Fryer, & Cox, 2005). Currently, methods to produce whole-muscle-like products from plant-based and microbial-based ingredients are scarce.

Meat consists of muscle fibre bundles, hierarchically assembled from fibrous protein complexes that immobilise endogenous water within their interstitial spaces (Sha & Xiong, 2020). It is the aggregated muscle fibres and connective tissue of cooked lean meat that provide its distinctive chewy texture, while the juiciness comes from the release of immobilised water during denaturation of protein complexes. Analogous to other natural constructs containing aligned fibres, such as wood, the mechanical strength of meat is inherently direction-dependent or anisotropic. These highly organised structural features contribute to the sensory profile of whole-muscle meat, which is appreciated by meat-eating consumers, and notoriously difficult to reproduce with proteins from alternative sources.

3-D food printing (3DFP) is an emerging technology for food structuring. The number of studies investigating 3D printing of meat analogues using plant proteins or hybridised with animal protein has been increasing recently (Ko et al., 2021; Lee et al., 2023; Qiu et al., 2023). In 3DFP, extrusion-based processes are most common, where paste-like materials are deposited as strands into shapes layer-by-layer according to a digital model. Factors influencing the success of extrusion-based 3DFP include the rheological and textural properties of the printing paste as well as external influences from the printing equipment, such as printing parameters and print design (Zhang et al., 2022). The printing paste should be able to flow through the nozzle with low force and set after deposition to maintain its shape, thereby exhibiting pseudoplastic (shear-thinning) rheological behaviour (Jiang et al., 2019).

Hydrocolloids can modify the rheology of the printing paste and improve the post-processing stability. Alginate, a polysaccharide derived mainly from brown algae, is a linear copolymer of $(1 \rightarrow 4)$-linked β-D-mannuronic acid (M) and α-L-guluronic acid (G) residues arranged in sequential blocks, which vary in composition and order depending on the source (Cardoso, Costa, & Mano, 2016; Ko et al., 2021). An abundance of G residues increases the rigidity of the molecular structure, while abundance of M residue confers a more flexible structure (Cao et al., 2020). Sodium alginate shows calcium-dependent gelation, whereby divalent Ca^{2+} crosslinks between G residues of anti-parallel chains into the so-called 'egg-box' conformation to form a thermoirreversible gel (Pawar, Lalitha, & Ruckmani, 2015). For extrusion-based 3D printing of meat analogues, alginate can perform as a viscosity enhancer and gelling agent at different stages of the process. In the printing paste, alginate increases viscosity giving viscoelastic, shear-thinning properties, which enable ease of extrusion and shape stability after deposition. After calcium-crosslinking, a flexible thermostable gel is formed that resists cooking, such as frying. Locust (carob) bean gum (LBG) is a neutral galactomannan that forms highly viscous solutions at low shear, which are strongly shear-thinning. It consists of linear $(1 \rightarrow 4)$-β-D-mannan chains, where single D-galactose substituents are linked to the main backbone by $(1 \rightarrow 6)$-α-glycosidic bonds. The galactose side chains of LBG offer synergistic viscosity enhancement and reduction of syneresis when mixed with other polymers such as sodium alginate to aid the printing process (Cheng, Cao, Liu, Mei, & Xie, 2022; Petitjean & Isasi, 2022).

Print design and printing parameters can be manipulated to influence the final texture and mechanical properties. Unidirectional alignment of fibres has been widely reported in biopolymer, polymer and composite printing materials within extrusion-based 3D printing processes (Mulholland, Goris, Boxleitner, Osswald, & Rudolph, 2018; Consul, Beuerlein, Luzha, & Drechsler, 2021; Gauss, Pickering, & Muthe, 2021; Rutzen et al., 2021) and mycoprotein fibres in ram extrusion (Miri et al., 2005). By adapting the toolpath, this principle could be exploited

to influence the microstructure of extrusion-printed meat analogues containing texturized protein fibrils within a hydrocolloid gel and provide anisotropic mechanical properties and a meat-like appearance and texture.

The aim of this study was to elucidate the structure and texture formation mechanisms during 3D extrusion-printing of pea protein and SCP-based meat analogues. Addition of SCP can complement the nutritional quality of pea protein. The effect of hydrocolloids and pea protein-SCP ratio on printing paste rheology and printability were studied using a controlled stress rheometer. Structural properties of printed, calcium-crosslinked analogues were assessed by x-ray microtomography, whereas direction-dependent textural properties were studied by bi-directional cutting tests and uniaxial compression.

2. Materials and methods

2.1. Materials

Texturized pea protein (TPP) (Hernis herneproteiini, Oy West Mills Ab, Jalasjärvi, Finland) was purchased from a local supermarket. The TPP nutritional content as stated by the manufacturer per 100 g was: Energy 1685 kJ / 400 kcal, Fat 9 g of which saturated fats 2 g, Carbohydrates 0 g of which sugars 0 g, Dietary fibre 1 g, Protein 79 g, Salt 2.5 g. TPP was processed into smaller fibrils. First, equal weight of TPP and water were combined and allowed to absorb for 2 h. Next, TPP was sheared using a Blendtec CTB2 blender equipped with a blunt cutting blade into smaller fibrils and sifted through a 1 mm mesh sieve. The sieved fibrils were oven-dried at 105 °C for 12 h and adjusted to 8% moisture content prior to use. Microbial single cell protein (SCP) was provided by Solar Foods (Solein, Solar Foods Oy, Lappeenranta, Finland). According to the manufacturer, the nutritional content of SCP per 100 g was: Energy 1680 kJ / 401 kcal, Carbohydrates 0 g of which sugars 0 g, Protein 68.5 g, Fat 10.2 g of which saturated fats 4.4 g, Dietary Fibre 17.5 g, Salt 0.13 g. Locust bean gum (LBG), sodium alginate (SA) and calcium lactate were purchased from Special Ingredients (Special Ingredients Ltd, Chesterfield, United Kingdom). Reverse osmosis water was used in all experiments.

2.2. Ingredient characterisation

2.2.1. Water holding capacity

The centrifugal water holding capacity (WHC) of protein ingredients (TPP, SCP) was determined according to AACC Method 56-20.01 (AACC, 2000). Briefly, 1 g of material was mixed with 10 mL of distilled water and incubated for 30 min at room temperature. The sample was centrifuged at 2000*g* for 10 min, supernatant decanted and the pellet water holding recorded in mass. SCP powder and TPP fibrils were analysed *as is*. As a control, TPP were dry milled into a powder with a Bamix hand blender equipped with a wet/dry processor (Bamix SwissLine, Mettlen, Switzerland).

2.2.2. Moisture content

The moisture contents of ingredients and crosslinked meat analogues were analysed with a halogen moisture analyser using a fast heating profile at 105 °C (MB120, Ohaus, Greifensee, Switzerland) as triplicate measurements.

2.3. Printing paste preparation

Pastes for printing were prepared according to ingredient composition in Table 1. First, concentrated SA and SA-LBG stock solutions were prepared by dispersing powder into water while mixing with a Blendtec CTB2 blender. After dispersing, the hydrocolloid solution was rapidly microwave-heated to 99 °C and allowed to cool to 4 °C before use. Next, a paste was formed by adding TPP and SCP into the hydrocolloid solution and hydrating at 4 °C for 12 h. After hydration, the paste was mixed

Table 1
Ingredient composition of the printing pastes.

Sample name	% w/w				
	Water	SA	LBG	TPP	SCP
SA+LBG-1	77.2	2.0	0.8	10.0	10.0
SA+LBG-2	77.2	2.0	0.8	15.0	5.0
SA-1	77.2	2.8		10.0	10.0
SA-2	77.2	2.8		15.0	5.0
M-SA+LBG-1	77.2	2.0	0.8	10.0	10.0
M-SA-1	77.2	2.8		10.0	10.0

TPP = Texturized pea protein; LBG = locust bean gum; SCP = single cell protein; SA = sodium alginate; M = moulded control.

using a SpeedMixer dual asymmetric centrifugal laboratory vacuum mixer system (DAC 1100.1 VAC-P vacuum mixer system, Synergy Devices Limited, High Wycombe, United Kingdom) for 10 min at 1600 rpm and 100% vacuum. Mixed pastes were allowed to cool to 4 °C and immediately tempered to 22 °C prior to printing or analyses.

2.4. Rheological measurements

The viscoelastic properties of printing pastes were determined by oscillatory stress sweep measurements using an AR-G2 controlled stress rheometer (TA Instruments, New Castle, DE, USA). The pastes were tempered to ambient temperature and measured at 22 °C using 20 mm diameter parallel stainless-steel plates with a gap of 1.5 mm. The sample was loaded, and excess paste was trimmed around the edges of the plate, and then the edge was covered with paraffin oil to prevent evaporation of water. After a 5-minute soaking time, the measurement started where the shear stress increased logarithmically from 0.01 Pa to 10000 Pa at a frequency of 0.1 Hz with five measurement points per decade. Three replicates were measured per sample type. Mean values of storage modulus G' corresponding to elastic behaviour, loss modulus G'' representing viscous behaviour and phase angle were extracted from the linear viscoelastic region (LVR). In addition, yield stress was determined for each paste. Yield stress was defined as the point where G' falls below 90% of its value in the linear viscoelastic region (Lille, Kortekangas, Heiniö, & Sozer, 2020).

2.5. Printing and post-processing of meat analogues

The meat analogues were 3D-printed as square slabs using an extrusion-based Foodini 3D Food Printer (Natural Machines, Barcelona, Spain) equipped with a stainless-steel ingredient capsule (100 mL) and nozzle of diameter 1.5 mm. Printing pastes were tempered to 22 °C and manually loaded into the capsules using a spatula, taking care to avoid formation of voids. The printing model was created using two complementary two-dimensional patterns in Scalable Vector Graphics (SVG) format that were assembled into a total of four alternating layers in the Foodini Creator software. Both two-dimensional SVG patterns consisted of a row of lines spaced 2 mm apart surrounded by a perimeter line covering an area of 100 × 100 mm. The lines within the frames were offset by 1 mm between layers. The toolpath was generated in Foodini Creator, whereby each line is deposited as a single 1.5 mm wide strand of printing paste layer-by-layer. In each layer the perimeter line was printed first followed by a rectilinear filling of the area inside the frame so that adjacent printed strands were in contact. The distance between layers was set to 1.4 mm to give a slight drag of the nozzle and compression of strands over the previous layer and to promote fibre alignment within the strands. Printing speed was set to 3200 mm/min. The toolpath is graphically represented in Fig. 1A, showing the parallel orientation, and staggering of strands between layers.

After completing the print, the weight of the slab was recorded to follow consistency of paste deposition between replicates. The printed slab was solidified by ionic crosslinking. First, a 5 % w/w solution of calcium lactate was sprayed over the surface, and then the slab was immersed into a bath containing an excess of the same solution and allowed calcium to diffuse throughout the structure for 24 h at 4° C. The crosslinked meat analogue slabs were vacuum-packed and stored at −18 °C.

In addition, moulded control samples were prepared by manually depositing 61 g of printing paste into a square mould with internal dimensions of 100 × 100 × 5.6 mm and levelling using a spatula. Preparation of printing paste, ionic crosslinking and storage for moulded controls was carried out identical to 3D-printed samples, as described above.

2.6. Textural characterisation

Textural properties of crosslinked meat analogues were measured using a TA.XT2i Texture Analyser (Stable Micro Systems Ltd, Godalming, Surrey, United Kingdom) equipped with a 30 kg load cell with a bi-directional cutting test and a uniaxial compression test. Crosslinked meat analogue slab samples were thawed overnight at 4 °C and then cut into squares with side length of 20 mm excluding the edges of the slab as shown in Fig. 1B. The surface of the sample pieces was dried by lightly patting with a paper towel and tempered to 22 °C, while kept covered before the measurement.

The directional mechanical properties of meat analogues were
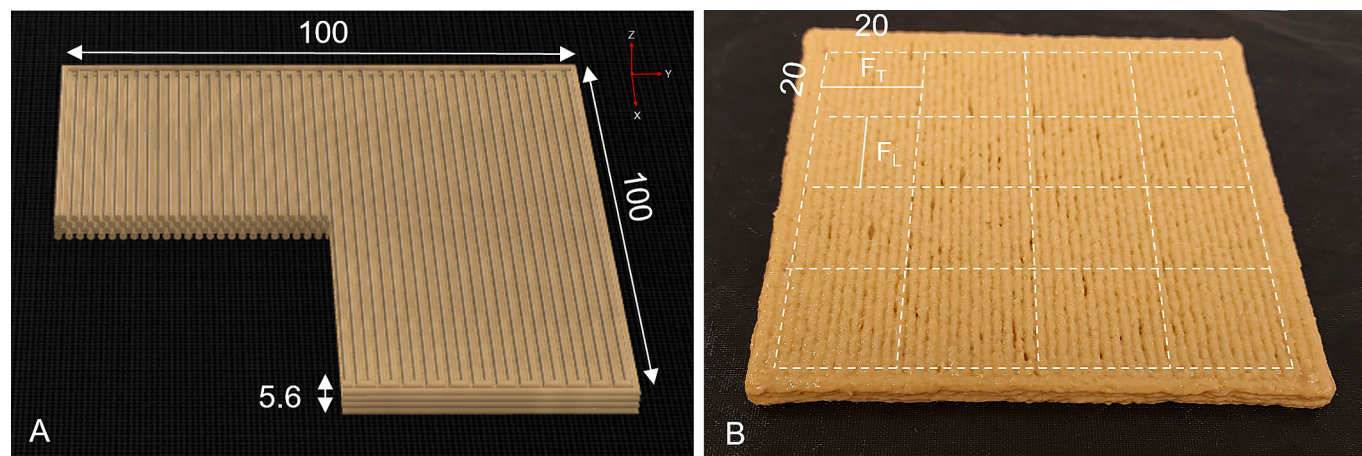
Fig. 1. A) Graphical representation with sectional view of the printed meat analogue slab showing interlayer staggering of print strands, dimensions in millimetres and the X, Y and Z axes in relation to the printed strands. B) Printed meat analogue slab before crosslinking with calcium lactate solution. Dashed lines show where samples for textural analysis were cut into 20 × 20 mm squares and solid lines indicate longitudinal (F_L) and transversal (F_T) directions in relation to printed strands.

assessed by a cutting test using a Warner Bratzler knife blade (HDP/BS) and a slotted blade insert. The prepared sample squares were placed over the slotted blade insert and sheared through the middle by the blade in either longitudinal or transversal direction relative to the printed strands using a test speed of 2 mm/s. The maximum cutting force (N) in transversal and longitudinal direction was recorded. The measurement was repeated at least 6 times in each direction. The anisotropy index (AI) according to Wittek, Karbstein, and Emin (2021) was calculated as the ratio of mean maximum transversal (F_T) and longitudinal (F_L) cutting force:

$$AI = F_T / F_L$$

Uniaxial compression test was carried out to determine hardness of the meat analogue sample squares. The test was performed with an aluminium cylindrical probe of 45 mm diameter at test speeds (pre-test, test and post-test speed) of 1 mm/s to 50% compression. Hardness was recorded as force at 50% compression. The measurement was performed on 7 replicate samples.

2.7. X-ray microtomography and image analysis

X-ray microtomography (XμCT) was used as a non-destructive testing method to reveal the internal structure and fibril alignment in meat analogue samples. The XμCT imaging was carried out using a Desktop 130 XμCT scanner (RX Solutions, Chavanod, France). For imaging, 3D-printed and moulded analogue samples were cut into 10 mm × 10 mm pieces, lyophilised, and attached onto the sample holder with tape before placing into the imaging chamber. The acceleration voltage was 40 keV with a 200 mA current. Imaging framerate was set at 6 1/s with 2 frame averaging giving a total of 1440 images per sample rotation. Voxel size was 5.2–6.5 μm. Each sample was scanned in triplicate. Porosity was determined using a local thickness transform giving the percentage of void space over the total volume of the sample (Hildebrand & Rüegsegger, 1997). The microtomography reconstructions were imported into the open-source ImageJ imaging software (Schneider, Rasband, & Eliceiri, 2012) and representative 2D images near the middle of the sample were selected and cropped to 1400x700 and 700x700 pixels for Z- and X-axis slices, respectively (Fig. 2). The output of the imaging process is a three-dimensional reconstruction of the X-ray attenuation values in the imaging area. The X-ray attenuation values in principle correlate with the density. In this case the air has low X-ray attenuation while the sample has high and, thus, it enables distinguishing the pore space from the other material.
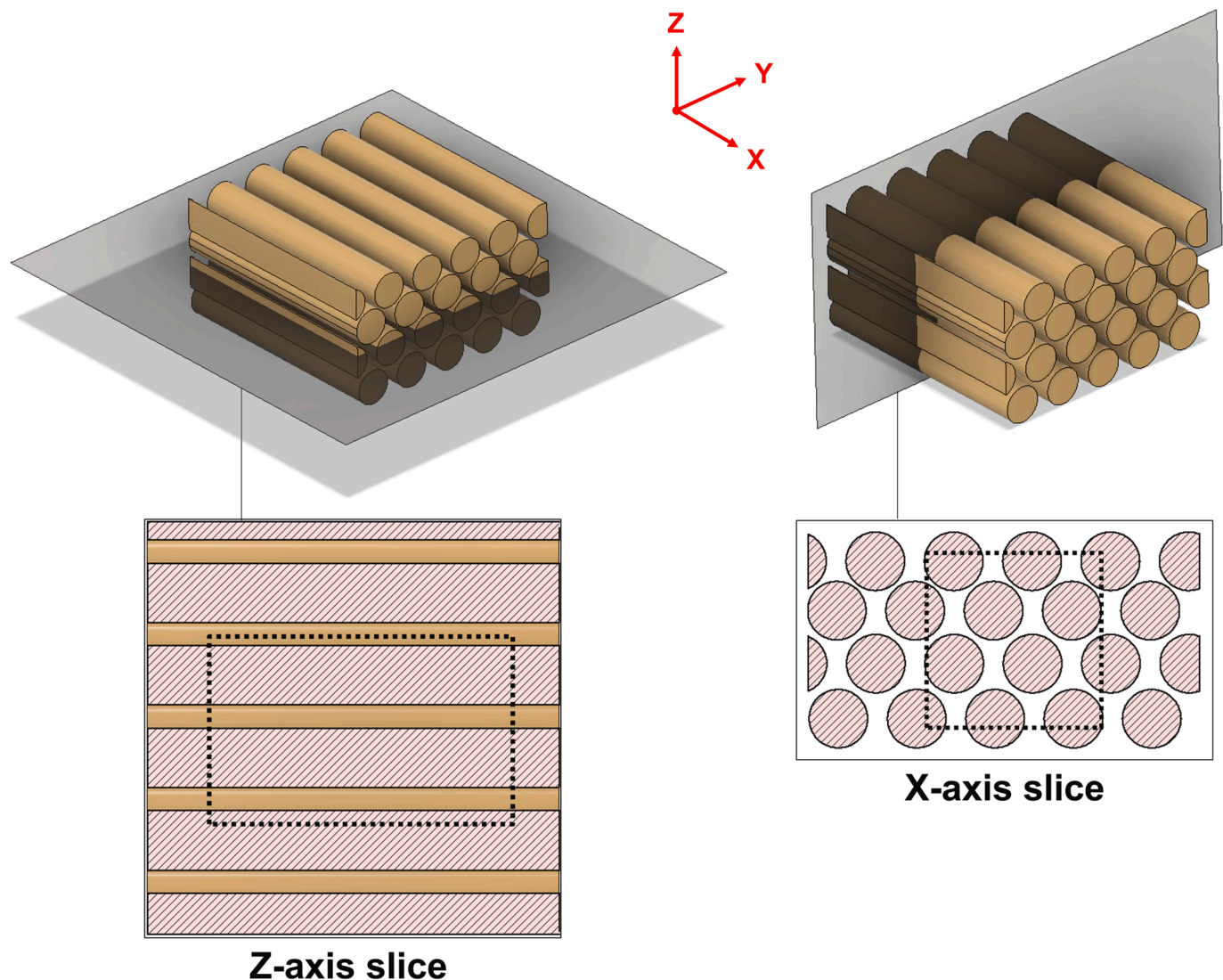

Fig. 2. Location of Z- and X-axis slices from the 3D x-ray microtomography images of meat analogue samples. The area delimited by the dashed line shows where 2D images were cropped.

2.8. Statistical analyses

Data were analysed with IBM SPSS Statistics version 28.0 (IBM Corporation, New York, USA). The significance of differences between samples were analysed with one-way analysis of variance (ANOVA) followed by a Games-Howell post hoc for data of unequal variance or Tukey's honestly significant difference (HSD) test for data with equal variance. Statistical significance was accepted at $P < 0.05$.

3. Results and discussion

3.1. Rheological properties of printing pastes

In all pastes, values of the storage modulus G' in the LVR ranged between 4000 and 6000 Pa and exceeded the loss modulus G'', indicating elastic-dominant, solid-like behaviour (Table 2). The G' values are a measure of the sample stiffness or gel strength at rest, which influences the ability to maintain the three-dimensional shape of the printed object after deposition, while G'' represents the energy spent to deform the printing paste during flow (Nijdam, LeCorre-Bordes, Delvart, & Schon, 2021). Furthermore, the phase angle values ranged between 21 and 26° indicating elastic nature. Phase angle can vary between 0 and 90° and is the ratio of the viscous to elastic effects with values below 45° describing elastic-dominant samples. The lower the phase angle, the more solid-like the sample is. All the measured printing pastes were qualitatively assessed as printable giving sufficient shape stability.

The presence of LBG in the printing paste had a greater effect on paste properties than the proportion of SCP to TPP. The G' values in both LBG-containing pastes were significantly higher at 5910–5497 Pa compared to SA alone with 4226–4049 Pa (P < 0.05). Moreover, LBG increased the yield stress significantly to 62.3–62.4 Pa from 24.7 to 39.2 Pa in samples containing SA alone. Yield stress is the point at which the material will yield and begin to flow or deform, and thus relates to the printing paste mechanical strength in maintaining shape of deposited layers. Therefore, LBG increased the mechanical rigidity of the printing paste and is expected to improve shape fidelity and stability after deposition. In accordance, Lille et al (2018) concluded that in pastes with similar G' values, the higher yield stress was a stronger determinant than G' of shape stability of the printed shape.

In line with our results, Lille et al. (2020) reported similar values of G' (4000–6000 vs 1000–8000 Pa) and yield stress (25–60 vs 10–60 Pa) of milk protein-wholegrain rye-based pastes that were printable with good shape stability using the same nozzle diameter (1.5 mm) (Lille et al., 2020). Zhu et al (2019) showed a linear correlation with the G' and flow stress ($G'=G''$) from stress sweep measurements of various printing pastes (e.g., tomato paste, mayonnaise, chicken pate) with extrusion pressure and printing stability, using a smaller nozzle (1.2 mm). Due to the more complex fluid flow during nozzle extrusion, which is not fully addressed by small-deformation rheological tests, G' as a parameter of the non-deforming state was shown not to correlate with extrusion pressure, nor with shape stability beyond tomato paste. Zhu et al (2019) reported flow stress values, the crossover points of G' and G'', of ~120 Pa for tomato paste, which are higher than the yield stress values reported in our study. The G' values of tomato paste were approximately 4000 Pa

with a yield stress point in the region of 40–50 Pa, which are in line with the values measured in our study. It must be stressed that the rheological measurements of complex particulate food materials are challenging and the results may depend on the method and instrument used as well as the shear history of the sample. It is also likely that slip in the form of wall-depletion was to some extent present in our measurements with a smooth-surfaced geometry (Hatzikiriakos, 2015). With this consideration, for the aqueous-based pastes in our study, a higher yield stress (LBG-containing paste) likely increased the force required for extrusion and improved shape stability of successive layers, while G' is a general indication of mechanical rigidity at rest. Furthermore, the fibrillar particles (from texturized pea protein), in the pastes may introduce artefacts to the measurements, making accurate prediction of printing performance based on rheological tests challenging.

The hydrocolloids used in this study, alginate and LBG, fall into the category of thickeners (viscosity enhancers) or gelling agents (ability to form a gel), respectively, based on their physical functionality. However, cross-linkable alginate performed a dual role of thickener and gelling agent. Selection of suitable hydrocolloids for extrusion-based 3D printing of meat analogues requires special consideration as different stages of the process (extrusion, deposition, post-processing, cooking) may require distinct rheological and mechanical properties from the paste, and its printing subsequently determines the physical properties of the final structure (Dick, Dong, Bhandari, & Prakash, 2021). For the deposition stage of the printing process, replacing a fraction of SA with LBG enhanced the paste properties by more efficient thickening (increase in G' and yield stress) but decreased the crosslinking gelling ability during post-processing in the final printed structure compared to SA alone.

Additionally, the water holding capacity (WHC) of SCP and fine and fibrillar TPP was determined: WHC of fibrillar TPP (3.9 ± 0.1 g/g) was significantly higher than fine TPP (2.9 ± 0.2 g/g) and SCP (3.0 ± 0.1 g/g) (P < 0.05). These results clearly show that the higher WHC of fibrillar TPP is linked to particle size and its spongy nature, which traps water and increases the volume fraction (discussed further in section 3.2). In all pastes, there is a trend for decreasing G' and increasing G'' when proportion of fibrillar TPP increases (although not statistically significant), which may be partly explained by differences in the WHC of ingredients through water distribution between the components of the paste.

3.2. Microstructural properties

Both printed and moulded meat analogue samples were lyophilised and scanned using the non-destructive X-ray micro tomography method to characterise the internal microstructure and visualise the orientation of pea protein fibrils (Fig. 3). Selected two-dimensional slices along the Z- and X-axes show areas of low density, or empty spaces, as dark and areas of higher density, or solid objects, as light structures. Two distinct types of constructs can be seen in light colours: cell wall-like structures consisting of desiccated hydrocolloid-SCP gel that envelope individual porous TPP fibrils (annotated with red arrows). During lyophilisation, the hydrocolloid-SCP gel shrunk and retracted from around TPP fibrils. This indicates that these two phases, TPP fibrils and hydrocolloid-SCP, adhere to each other poorly and do not interact. It is likely that the surface hydrophobicity of TPP fibrils is high due to thermal denaturation and exposure of hydrophobic sites, turning it incompatible with hydrophilic hydrocolloids (Osen, Toelstede, Wild, Eisner, & Schweiggert-Weisz, 2014). In general, the length of TPP fibrils (2–5 mm) exceeds their diameter (<1mm), giving them an aspect ratio (length/diameter) >1. The length also exceeds the diameter of the printing nozzle (1.5 mm). The 2D images reveal the porous nature of TPP fibrils. However, there were also spherical fibrils present with an aspect ratio closer to 1.

There was a fundamental difference in TPP fibril orientation between the printed and moulded samples: the printing process induced fibril alignment along the printing path, while moulding produced random

Table 2
Viscoelastic properties of printing pastes as determined by stress sweep measurements. The storage modulus G', loss modulus G'' and phase angle are shown as mean values ± standard deviation from the linear viscoelastic region (LVR). Columns not sharing a letter are significantly different (P < 0.05).

Sample	G' (Pa)	G'' (Pa)	Phase angle (°)	Yield stress (Pa)
SA+LBG-1	5910 ± 502[a]	2338 ± 151[b]	21.6 ± 0.5[c]	62.3 ± 0.1[a]
SA+LBG-2	5497 ± 383[a]	2585 ± 208[a]	25.2 ± 0.4[a]	62.4 ± 0.1[a]
SA-1	4226 ± 492[b]	1799 ± 149[c]	23.2 ± 2.1[b]	24.7 ± 0.1[c]
SA-2	4049 ± 471[b]	1940 ± 210[c]	25.6 ± 0.8[a]	39.2 ± 0.1[b]

Z-axis slice **X-axis slice**

SA+LBG-1

Porosity (%) = 74 ± 1 ab

SA+LBG-2

Porosity (%) = 73 ± 3 b

SA-1

Porosity (%) = 76 ± 0 b

SA-2

Porosity (%) = 75 ± 1 ab

M-SA+LBG-1

Porosity (%) = 79 ± 1 a

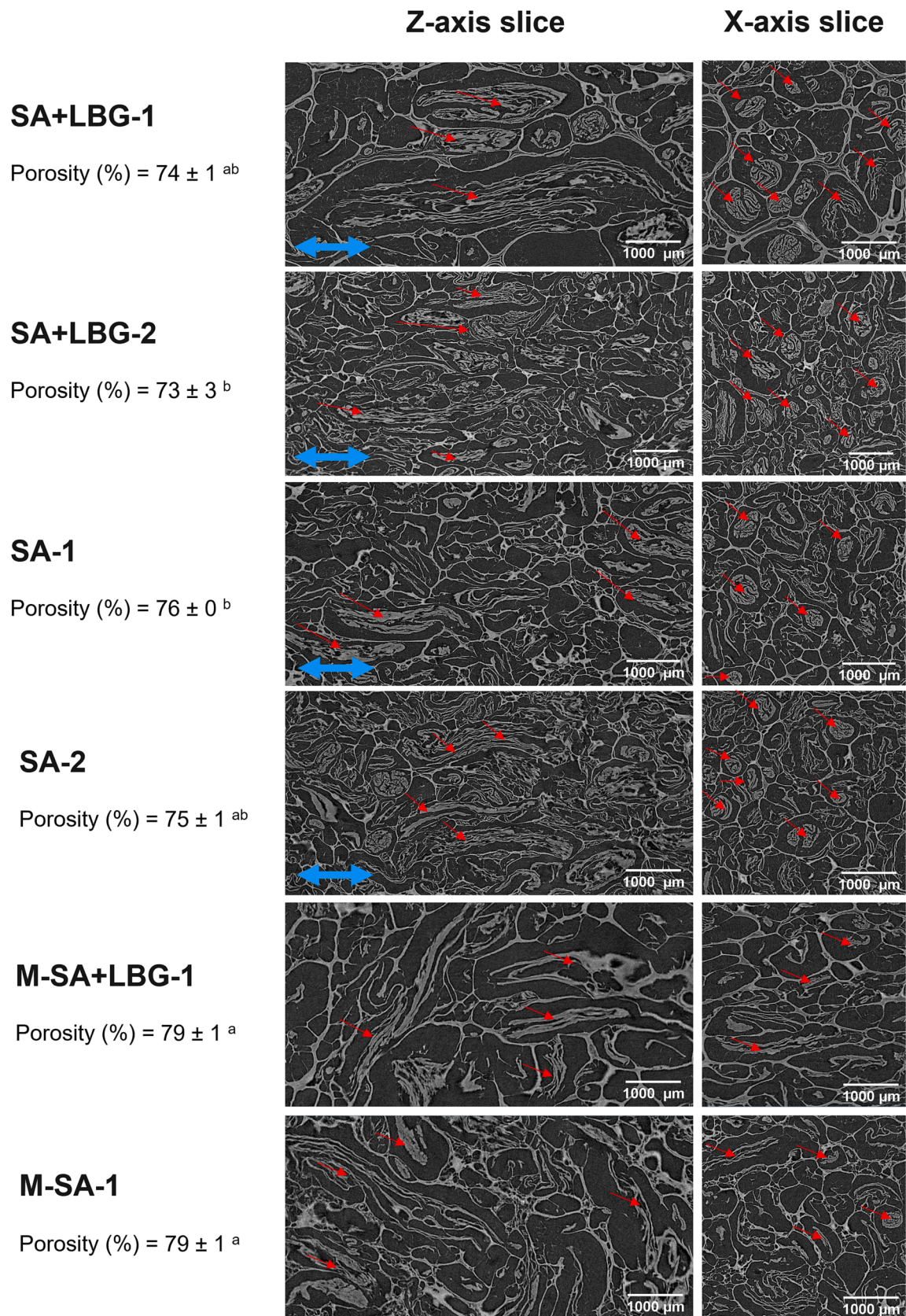**M-SA-1**

Porosity (%) = 79 ± 1 a

Fig. 3. X-ray microtomography 2D images and porosity (%) values of lyophilised meat analogues along the Z- and X-axes. Values not sharing a letter are statistically different (P < 0.05). Blue arrows show direction of nozzle movement in printed samples. Red arrows point to some of the TPP fibrils. Samples with M-prefix are moulded and do not contain printed strands. Scale bar is 1000 μm. (For interpretation of the references to colour in this figure legend, the reader is referred to the web version of this article.)

orientation across all planes. Qualitatively assessed, the Z-axis slices of printed samples (Fig. 3) show a longitudinal view of TPP fibrils, which indicated a preferential alignment in the direction of printing nozzle moving in the X-plane (blue arrows signify direction of nozzle movement). From the X-axis slices (Fig. 3) only the cross-sectional view of fibrils can be seen demonstrating that they were oriented along the X-axis and contained within each printed layer. On the contrary, Z-axis slices of moulded samples (Fig. 3), show random alignment of fibrils in the x-y orientation. Furthermore, X-axis slices of moulded samples (Fig. 3) show a mixed population of both the cross-sectional and longitudinal views of the fibrils, demonstrating how fibrils occupy the volume with random orientation. Closer inspection (results not shown) revealed that moulding caused fibrils to cross all planes in ×, y and z.

The porosity of moulded samples (Fig. 3) was significantly higher at 79% than some printed samples (SA + LBG-2, SA-1) at 73–76% (P < 0.05). Although not statistically significant, the trend pointed to lower porosity in the other printed samples (SA + LBG-1, SA-2) at 74–75% compared to moulded samples. However, there were no statistically significant differences in porosity between printed samples. Presumably, moulding led to less efficient packing as randomly oriented fibrils overlap and entangle each other creating more voids than in printed samples.

This principle of printing-induced fibril alignment and random orientation during moulding is illustrated in Fig. 4. Fibrils contained in the paste align according to the flow field and are deposited within individual print strands, which fuse during crosslinking into a continuous gel embedding the aligned fibrils. On the other hand, in manually moulded samples fibrils point to different directions. Analogous to the extrusion-based 3D printing in this study, Miri et al. (2005) reported a high degree of mycoprotein filament alignment in the direction of flow during ram or piston extrusion. It was shown that fibre alignment is determined by the extruder die size rather than applied shear rate which signifies that fibres align at the die entry region rather than by shearing within the die. The 2D images in Fig. 3 illustrate how the printing process can determine the alignment of fibrils through a defined tool-path: parallel strands staggered between layers leads to unidirectional alignment whereas moulding creates isotropic, random fibril orientation.

3.3. Physical properties of printed analogues

Physical properties of printed analogues as pre-crosslinking slab weight and post-crosslinking moisture content are presented in Table 3. The weights of printed slabs prior to crosslinking with calcium lactate solution showed good repeatability of the printing process with equal slab weights at around 60 g (P < 0.05). After crosslinking, the moisture contents did not differ significantly between the samples with 71–72 % moisture, apart from sample SA + LBG-2 with 76% moisture (P < 0.05). It is likely that a combination effect of higher TPP content and LBG presence increased the water absorption capacity and reduced syneresis of the printed structure leading to more water absorbing during the crosslinking process. Furthermore, galactomannans such as LBG are known for their ability to reduce syneresis, which may occur when alginate shrinks during the crosslinking process (Drageta et al., 2001; Xu, Ye, Zuo, & Fang, 2022). On the other hand, both moulded controls with randomly oriented fibrils had slightly elevated moisture content compared to their printed counterparts. This suggests that random fibril orientation also increases water absorption capacity through less tight packing increasing porosity and capillary action.

3.4. Textural properties of analogues

Textural properties of printed, crosslinked analogues were

Table 3
The pre-crosslinking printed meat analogues' slab weight and moisture content of crosslinked meat analogues. Columns not sharing a letter are significantly different (P < 0.05).

Sample	Printed slab weight, pre-crosslinking (g)	Moisture content (%), post-crosslinking
SA+LBG-1	60.8 ± 0.4[a]	72.9 ± 0.3[b]
SA+LBG-2	60.7 ± 0.3[a]	76.1 ± 0.3[ac]
SA-1	60.6 ± 0.2[a]	71.9 ± 0.3[bd]
SA-2	60.8 ± 0.3[a]	72.7 ± 1.5[bcd]
M-SA+LBG-1	*	74.9 ± 0.2[d]
MSA-1	*	76.0 ± 2.1[bcd]

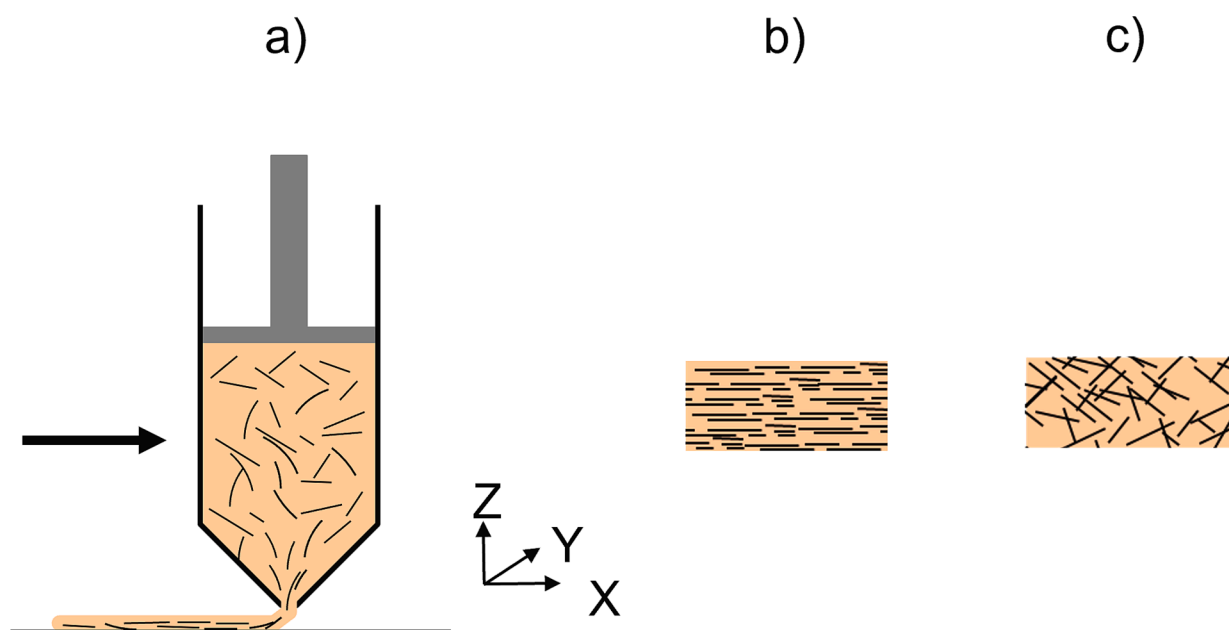*61.0 g of printing paste were used for moulded samples.

Fig. 4. A) the principle of fibril alignment during extrusion-based 3d printing of fibre-containing printing paste, b) 3-d printing-induced fibril orientation along x-axis in meat analogue, c) random orientation of fibrils in moulded meat analogue.

characterised by measuring the direction-dependent or anisotropic properties as cutting force in the in-plane transversal (F^T) or longitudinal (F^L) orientations relative to the printed strand (Fig. 5), and gel hardness through uniaxial compression testing (Fig. 6). The difference between transverse and longitudinal cutting force can be represented as the anisotropy index (Fig. 7), where a value of 1 indicates uniform texture and values above or below 1 show anisotropy in texture. The larger the difference between longitudinal and transversal cutting force, the more anisotropic the texture is and may indicate fibrous texture and meat-like properties (Osen et al., 2014). Some authors refer to F^T / F^L as 'degree of texturization' (Chen, Wei, Zhang, & Ojokoh, 2010; Lee et al., 2023).

In all printed analogues, $F^T > F^L$ indicating anisotropic textural properties in the x-y or in-plane orientation (P < 0.05) (Fig. 5). In samples containing LBG, the mean F^T decreased from 20.6 N to 16.5 N when the SCP:TPP ratio decreased from 50:50 to 25:75, although the difference was not statistically significant due to a high standard deviation (P < 0.05). Higher content of heterogeneous TPP fibrils increases textural variation in samples compared to the fine, homogeneous powdered SCP. Similarly, F^L decreased from 12.4 N to 8.1 N with decreasing SCP content (P < 0.05) (Fig. 5). The cutting force in printed meat analogue gels was determined by the interplay between embedded TPP fibrils, and a continuous gel composed of hydrocolloids and finer SCP. At higher SCP content, the continuous gel became firmer with subsequently higher cutting force in both directions. Subsequently, the anisotropy index increased from 1.7 to 2.5 with increasing TPP fibril content demonstrating that with less SCP present, the continuous gel weakened and the TPP fibrils dominated the structural properties, promoting anisotropy. Equally, hardness decreased from 81.6 N to 56.8 N as TPP content increased (P < 0.05) (Fig. 6).

In alginate-only printed analogues, the overall cutting forces were significantly higher than in LBG-containing samples with F^T values of 30.3–29.8 N, and F^L of 21.7 – 20.7 N for SCP:TPP ratios 50:50 and 25:75, respectively (P < 0.05) (Fig. 5). Higher cutting force values are explained by higher content of cross-linked Ca-alginate present producing a stronger continuous gel, which dominates texture. However, decreasing SCP:TPP ratio had no influence on cutting force. Consequently, the AI values remained at 1.4 with both samples, still indicating anisotropy in texture. This could imply that the source of anisotropy in alginate-only samples was the incomplete fusion of individual printing lines, rather than fibril alignment. Yet, the textural variation increased with a lower SCP:TPP ratio. The trend pointed to lower cutting forces and higher anisotropy when SCP content decreased. Furthermore, hardness decreased significantly from 80.7 N to 68.5 N with increasing

TPP content (P < 0.05). Presumably, SCP at higher concentration strengthens the continuous alginate gel, while at lower concentration TPP begins to dominate the structural properties and increase anisotropy.

Moulded controls demonstrated isotropic textural properties since the cutting force was similar in both directions (P < 0.05). AI values were also close to 1 at 1.0 and 0.8. The cutting force and hardness values were significantly lower compared to their printed counterparts. The random orientation of TPP fibrils with respect to all axes disrupts the continuous gel, which leads to a less tight packing. This is evident as a higher porosity, as determined from X-ray microtomography imaging, and moisture content after crosslinking due to increased capillary action (Fig. 3, Table 3). The moulded control illustrates the significance of TPP fibril alignment on the anisotropic properties. In 3D printing of individual strands layer-by-layer, structural anisotropy could be created along all x, y, and z axes. The typical reasons include incomplete fusion and porosity between parallel printed strands or by uniaxial alignment of reinforcing fibres (Consul et al., 2021). It must be noted that anisotropy resulting from incomplete fusion between parallel strands, as opposed to preferential alignment of protein fibrils, cannot be excluded using a moulded control in cutting tests. However, moulded samples appear to have lower flexural strength when folded leading to cracking compared to 3D printed samples folded in the longitudinal direction (See section 3.5), suggesting that fibre orientation, not printing lines or moulding, has an influence on mechanical properties of meat analogues in this study.

Overall, in both LBG-containing and alginate-only analogues, increasing content of TPP fibrils generally decreased hardness and cutting forces. This suggests a weak or non-existent adhesion between gel matrix polymers and surface of TPP fibrils, since the fibrils do not show a reinforcing effect (Unterweger, Duchoslav, Stifter, & Fürst, 2015). In addition, the X-ray microtomography images support the conclusion of weak interaction between gel matrix and TPP fibrils (Fig. 3). In this regard, heavily denatured, texturized TPP fibrils can be considered as inactive filler particles embedded in a crosslinked alginate gel with or without LBG, whereby mechanical properties are influenced by volume fraction of the filler and its length, diameter, and aspect ratio (Chen & Dickinson, 1999).

Bi-directional cutting tests have been used extensively to characterise anisotropic textural properties of high moisture extruded meat analogues and recently also in 3D printed meat analogues (Lee et al., 2023). However, the measuring parameters used vary, which makes direct comparison of values difficult. On a general level, cutting forces are
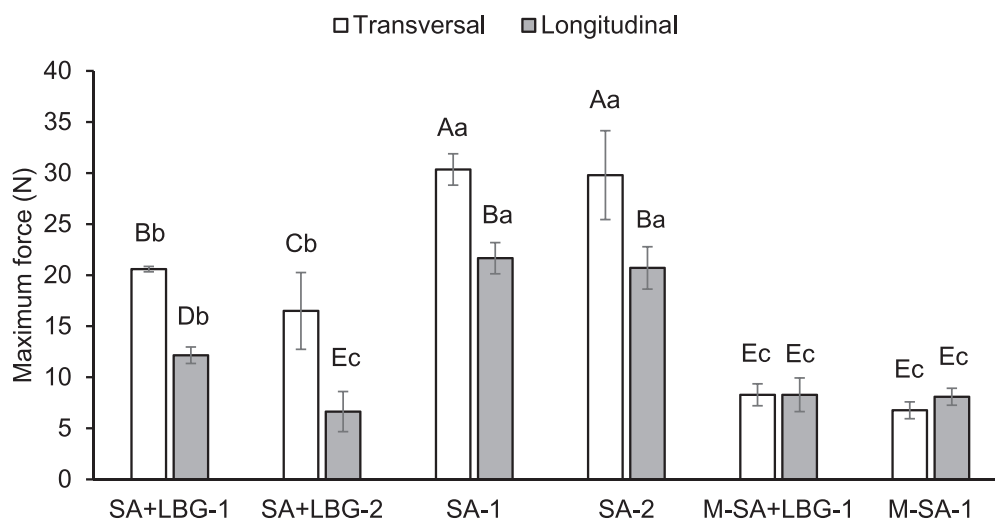

Fig. 5. The maximum cutting force required for meat analogues in the transversal and longitudinal orientation. Results are shown as mean of 6 replicate measurements ± standard deviation. Different uppercase letters indicate significant differences between means within the same column group, while different lower-case letters denote significant differences among the column groups in the same cutting direction (F_T or F_L) (P < 0.05).
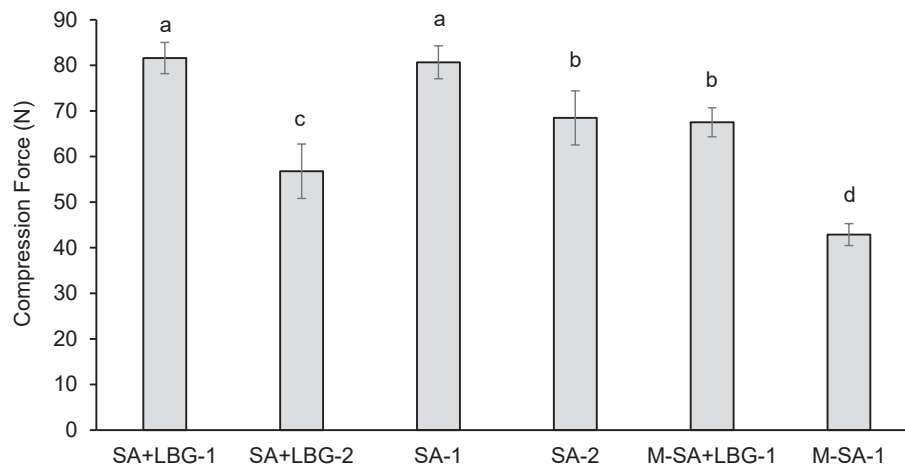
Fig. 6. The maximum force required for 50% compression of original height in crosslinked meat analogues. Results are shown as mean ± standard deviation of 7 replicate measurements. Means within each group not sharing a letter are significantly different (P < 0.05).
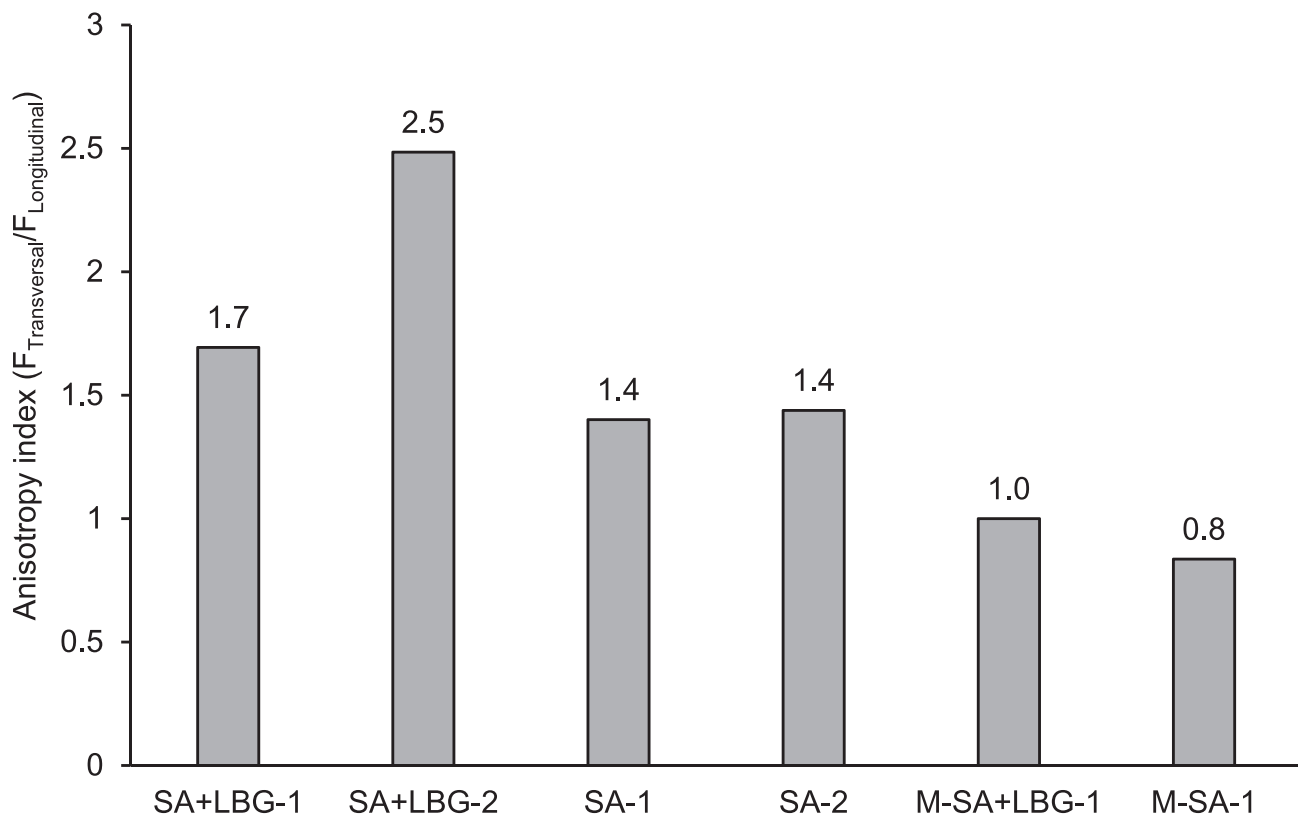

Fig. 7. The anisotropy index of meat analogues as a ratio of the mean maximum transversal and longitudinal cutting force.

higher when the blade cuts perpendicular to a fibrillar structure, and lower when it cuts longitudinally between the fibres (Zahari et al., 2020). Depending on the high moisture extruded sample matrix, formed fibrils may take on a characteristic V-shape in the flow field, which vary in angle. Subsequently, orientation of fibril in relation to the cutting blade vary, whereas F^T and F^L are defined the same in relation to direction of flow. Nevertheless, AI values can be compared since instrument-specific influences are absent. AI values reported in the literature are generally in line or lower than the present study. Wittek et al. (2021) reported highest AI value of 1.6 for soy protein isolate-whey protein concentrate extrudate. In 3D printed surimi-carrageenan and soy protein isolate-methylcellulose meat analogues with parallel strands

(nozzle sizes 1.1–2 mm), AI values of 1.2–1.8 were reported (Lee et al., 2023).

3.5. Appearance

The visual appearance of both 3D-printed and moulded crosslinked meat analogues is shown in Fig. 8 when folded in the longitudinal and transversal direction. In the longitudinal view (Fig. 8, top row) a fibrous internal structure can be seen because of TPP fibrils being embedded in a matrix of hydrocolloid(s) and single cell protein. Qualitatively, 3D-printed samples appear to have fibrils oriented according to the direction of the printing nozzle compared to moulded samples, although they
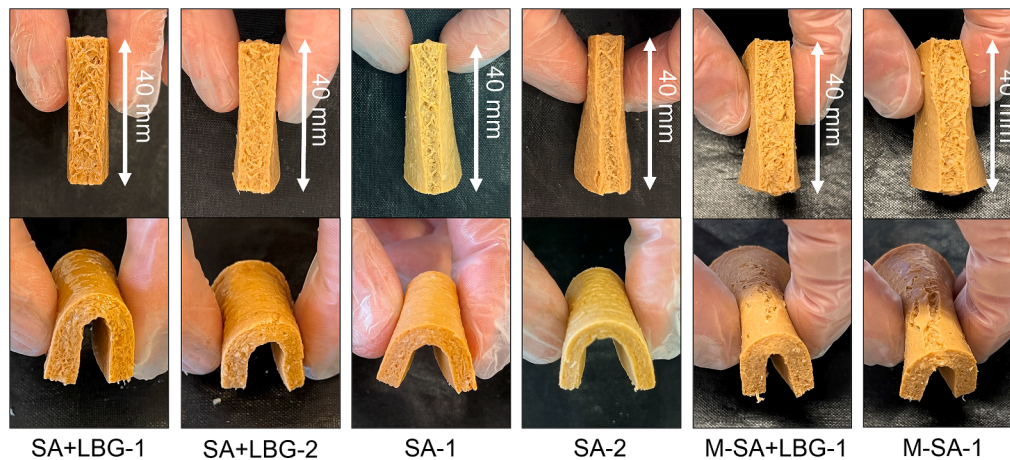
Fig. 8. Appearance of crosslinked meat analogues folded in longitudinal direction to demonstrate fibrous character (top row) and in transversal direction to illustrate flexural strength (bottom row). In the top row, a shallow cut was introduced to encourage a clean fold line. Sample pieces were 40 × 40 mm. Samples with M-prefix were prepared by moulding.

are pulled to either side due to folding. The appearance changes to a finer fibrillar structure when the proportion of TPP is increased and SCP decreased (Fig. 8, SA + LBG-2, SA-2) due to lesser colour contrast between SCP and TPP. Individual TPP fibrils become visually less distinct against a similar colour background. With a higher proportion of SCP, lighter coloured TPP strands stand out from the darker background of a hydrocolloid-SCP matrix. Samples containing LBG (Fig. 8, SA + LBG-1&2, M−SA + LBG-1) also appear coarser compared to those containing sodium alginate alone (Fig. 8, SA-1&2, M−SA−1). All 3D-printed analogues show strong flexural strength without cracking when folded across in the transversal direction, illustrating the anisotropic character created by printing of strands and the directional alignment of TPP fibrils. On the other hand, moulded samples have a propensity to crack at the top showing an overall lower flexural strength.

4. Conclusions

This study demonstrated the feasibility of extrusion-based 3D food printing for creating anisotropic meat analogues from TPP and SCP with the help of hydrocolloids. Pea protein fibrils were incorporated into hydrocolloid-SCP pastes and formed into shape by 3-D printing and moulding. The 3-D printing process led to unidirectional alignment of pea protein fibrils and created anisotropic textural properties compared to moulding which resulted in random orientation of fibrils and isotropic texture. Addition of LBG increased the mechanical rigidity of the printing paste with benefits to shape fidelity but decreased mechanical strength of crosslinked meat analogues compared to SA alone. Higher SCP content increased hardness and cutting force of the continuous gel and decreased the AI. These findings support further development of free-form 3D printed meat analogues based on alternative proteins that can provide some of the desired qualities of whole-muscle meat cuts. Furthermore, the meat analogues studied widen the applications for microbial SCP in novel food structures as a complete protein source for improved food security and sustainability. In future work, the effect of larger nozzle diameter and longer high aspect ratio fibrils could be explored as a higher throughput method to create meat-like fibrous gels.

CRediT authorship contribution statement

Alex Calton: Conceptualization, Methodology, Investigation, Formal analysis, Visualization, Writing – original draft. **Martina Lille:** Conceptualization, Methodology, Supervision, Writing – review & editing. **Nesli Sozer:** Conceptualization, Supervision, Funding acquisition, Project administration, Writing – review & editing.

Declaration of Competing Interest

The authors declare that they have no known competing financial interests or personal relationships that could have appeared to influence the work reported in this paper.

Data availability

Data will be made available on request.

References

AACC. Hydration Capacity of Pregelatinized Cereal Products. In *Approved Methods of Analysis*, 11th ed. AACCI Method 56-20.01; American Association of Cereal Chemists International: St. Paul, MN, USA, 1999.

Cao, L., Lu, W., Mata, A., Nishinari, K., & Fang, Y. (2020). Egg-box model-based gelation of alginate and pectin: A review. *Carbohydrate Polymers, 242*. https://doi.org/10.1016/j.carbpol.2020.116389

Caporgno, M. P., Böcker, L., Müssner, C., Stirnemann, E., Haberkorn, I., Adelmann, H., … Mathys, A. (2020). Extruded meat analogues based on yellow, heterotrophically cultivated Auxenochlorella protothecoides microalgae. *Innovative Food Science and Emerging Technologies, 59*, 102275. 10.1016/j.ifset.2019.102275.

Cardoso, M. J., Costa, R. R., & Mano, J. F. (2016). Marine origin polysaccharides in drug delivery systems. *Marine Drugs, 14*(2), 1–27. https://doi.org/10.3390/md14020034

Chen, F. L., Wei, Y. M., Zhang, B., & Ojokoh, A. O. (2010). System parameters and product properties response of soybean protein extruded at wide moisture range. *Journal of Food Engineering, 96*(2), 208–213. https://doi.org/10.1016/j.jfoodeng.2009.07.014

Chen, J., & Dickinson, E. (1999). Effect of surface character of filler particles on rheology of heat-set whey protein emulsion gels. *Colloids and Surfaces B: Biointerfaces, 12* (3–6), 373–381. https://doi.org/10.1016/S0927-7765(98)00091-5

Cheng, H., Cao, J., Liu, W., Mei, J., & Xie, J. (2022). Characterization of Sodium Alginate—Locust Bean Gum Films Reinforced with Daphnetin Emulsions for the Development of Active Packaging. *Polymers, 14*(4). https://doi.org/10.3390/polym14040731

Consul, P., Beuerlein, K. U., Luzha, G., & Drechsler, K. (2021). Effect of extrusion parameters on short fiber alignment in fused filament fabrication. *Polymers, 13*(15). https://doi.org/10.3390/polym13152443

Cornet, S. H. V., Snel, S. J. E., Schreuders, F. K. G., van der Sman, R. G. M., Beyrer, M., & van der Goot, A. J. (2022). Thermo-mechanical processing of plant proteins using shear cell and high-moisture extrusion cooking. *Critical Reviews in Food Science and Nutrition, 62*(12), 3264–3280. https://doi.org/10.1080/10408398.2020.1864618

Dekkers, B. L., Boom, R. M., & van der Goot, A. J. (2018). Structuring processes for meat analogues. *Trends in Food Science and Technology, 81*, 25–36. https://doi.org/10.1016/j.tifs.2018.08.011

Dick, A., Dong, X., Bhandari, B., & Prakash, S. (2021). The role of hydrocolloids on the 3D printability of meat products. *Food Hydrocolloids, 119*, 106879. 10.1016/j.foodhyd.2021.106879.

Drageta, K. I., GåserØd, O., Aunea, I., Andersen, P. O., Storbakken, B., Stokke, B. T., & SmidsrØd, O. (2001). Effects of molecular weight and elastic segment flexibility on syneresis in Ca-alginate gels. *Food Hydrocolloids, 15*(4–6), 485–490. https://doi.org/10.1016/S0268-005X(01)00046-7

Ercili-Cura, D., Hakamies, A., Sinisalo, L., Vainikka, P., & Pitkanen, J. (2020). Food out of thin air. *Food Science and Technology, 34*(2), 44–48. https://doi.org/10.1002/fsat.3402_12.x

Gauss, C., Pickering, K. L., & Muthe, L. P. (2021). The use of cellulose in bio-derived formulations for 3D/4D printing: A review. *Composites Part C: Open Access, 4*. https://doi.org/10.1016/j.jcomc.2021.100113

Petitjean, M., & Isasi, J. R. (2022). Locust Bean Gum, a Vegetable Hydrocolloid with Industrial and Biopharmaceutical Applications. *Molecules, 27*(23), 8265. https://doi.org/10.3390/molecules27238265

Hatzikiriakos, S. G. (2015). Slip mechanisms in complex fluid flows. *Soft Matter, 11*, 7851–7856. https://doi.org/10.1039/C5SM01711D

Herz, E., Herz, L., Dreher, J., Gibis, M., Ray, J., Pibarot, P., … Weiss, J. (2021). Influencing factors on the ability to assemble a complex meat analogue using a soy-protein-binder. *Innovative Food Science and Emerging Technologies, 73*. https://doi.org/10.1016/j.ifset.2021.102806

Hildebrand, T., & Rüegsegger, P. (1997). A new method for the model-independent assessment of thickness in three-dimensional images. *Journal of Microscopy, 185*(1), 67–75. https://doi.org/10.1046/j.1365-2818.1997.1340694.x

Jiang, H., Zheng, L., Zou, Y., Tong, Z., Han, S., & Wang, S. (2019). 3D food printing: main components selection by considering rheological properties. *Critical Reviews in Food Science and Nutrition, 59*(14), 2335–2347. https://doi.org/10.1080/10408398.2018.1514363

Ko, H. J., Wen, Y., Choi, J. H., Park, B. R., Kim, H. W., & Park, H. J. (2021). Meat analog production through artificial muscle fiber insertion using coaxial nozzle-assisted three-dimensional food printing. *Food Hydrocolloids, 120*. https://doi.org/10.1016/j.foodhyd.2021.106898

Lee, S. H., Kim, H. W., & Park, H. J. (2023). Integrated design of micro-fibrous food with multi-materials fabricated by uniaxial 3D printing. *Food Research International, 165*. https://doi.org/10.1016/j.foodres.2023.112529

Lille, M., Kortekangas, A., Heiniö, R. L., & Sozer, N. (2020). Structural and textural characteristics of 3D-Printed protein- and dietary fibre-Rich snacks made of milk powder and wholegrain rye flour. *Foods, 9*(11). https://doi.org/10.3390/foods9111527

Lille, M., Nurmela, A., Nordlund, E., Metsä-Kortelainen, S., & Sozer, N. (2018). Applicability of protein and fiber-rich food materials in extrusion-based 3D printing. *Journal of Food Engineering, 220*, 20–27. https://doi.org/10.1016/j.jfoodeng.2017.04.034

Miri, T., Barigou, M., Fryer, P. J., & Cox, P. W. (2005). Flow induced fibre alignment in Mycoprotein paste. *Food Research International, 38*(10), 1151–1160. https://doi.org/10.1016/j.foodres.2005.04.005

Mulholland, T., Goris, S., Boxleitner, J., Osswald, T. A., & Rudolph, N. (2018). Process-induced fiber orientation in fused filament fabrication. *Journal of Composites Science, 2*(3), 1–14. https://doi.org/10.3390/jcs2030045

Nijdam, J. J., LeCorre-Bordes, D., Delvart, A., & Schon, B. S. (2021). A rheological test to assess the ability of food inks to form dimensionally stable 3D food structures. *Journal of Food Engineering, 291*, 110235. 10.1016/j.jfoodeng.2020.110235.

Osen, R., Toelstede, S., Wild, F., Eisner, P., & Schweiggert-Weisz, U. (2014). High moisture extrusion cooking of pea protein isolates: Raw material characteristics, extruder responses, and texture properties. *Journal of Food Engineering, 127*, 67–74. https://doi.org/10.1016/j.jfoodeng.2013.11.023

Pawar, H. A., Lalitha, K. G., & Ruckmani, K. (2015). Alginate beads of Captopril using galactomannan containing Senna tora gum, guar gum and locust bean gum. *International Journal of Biological Macromolecules, 76*, 119–131. https://doi.org/10.1016/j.ijbiomac.2015.02.026

Qiu, Y., McClements, D. J., Chen, J., Li, C., Liu, C., & Dai, T. (2023). Construction of 3D printed meat analogs from plant-based proteins: Improving the printing performance of soy protein- and gluten-based pastes facilitated by rice protein. *Food Research International, 167*. https://doi.org/10.1016/j.foodres.2023.112635

Ritala, A., Häkkinen, S. T., Toivari, M., & Wiebe, M. G. (2017). Single cell protein-state-of-the-art, industrial landscape and patents 2001–2016. *Frontiers in Microbiology, 8*. https://doi.org/10.3389/fmicb.2017.02009

Rutzen, M., Lauff, P., Niedermeier, R., Fischer, O., Raith, M., Grosse, C. U., Weiss, U., Peter, M. A., & Volkmer, D. (2021). Influence of fiber alignment on pseudoductility and microcracking in a cementitious carbon fiber composite material. *Materials and Structures/Materiaux et Constructions, 54*(2). https://doi.org/10.1617/s11527-021-01649-2

Sha, L., & Xiong, Y. L. (2020). Plant protein-based alternatives of reconstructed meat: Science, technology, and challenges. *Trends in Food Science and Technology, 102*, 51–61. https://doi.org/10.1016/j.tifs.2020.05.022

Schneider, C. A., Rasband, W. S., & Eliceiri, K. W. (2012). Image to ImageJ: 25 years of image analysis. *Nature methods. Nature Methods, 9*(7), 671–675.

Sillman, J., Nygren, L., Kahiluoto, H., Ruuskanen, V., Tamminen, A., Bajamundi, C., … Ahola, J. (2019). Bacterial protein for food and feed generated via renewable energy and direct air capture of CO2: Can it reduce land and water use? *Global Food Security, 22*, 25–32. 10.1016/j.gfs.2019.09.007.

Unterweger, C., Duchoslav, J., Stifter, D., & Fürst, C. (2015). Characterization of carbon fiber surfaces and their impact on the mechanical properties of short carbon fiber reinforced polypropylene composites. *Composites Science and Technology, 108*, 41–47. https://doi.org/10.1016/j.compscitech.2015.01.004

Willett, W., Rockström, J., Loken, B., Springmann, M., Lang, T., Vermeulen, S., … Murray, C. J. L. (2019). Food in the Anthropocene: the EAT–Lancet Commission on healthy diets from sustainable food systems. *The Lancet, 393*(10170), 447–492. 10.1016/S0140-6736(18)31788-4.

Wittek, P., Karbstein, H. P., & Emin, M. A. (2021). Blending proteins in high moisture extrusion to design meat analogues: Rheological properties, morphology development and product properties. *Foods, 10*(7). https://doi.org/10.3390/foods10071509

Xu, X., Ye, S., Zuo, X., & Fang, S. (2022). Impact of Guar Gum and Locust Bean Gum Addition on the Pasting, Rheological Properties, and Freeze–Thaw Stability of Rice Starch Gel. *Foods, 11*(16), 2508. https://doi.org/10.3390/foods11162508

Zahari, I., Ferawati, F., Helstad, A., Ahlström, C., Östbring, K., Rayner, M., & Purhagen, J. K. (2020). Development of high-moisture meat analogues with hemp and soy protein using extrusion cooking. *Foods, 9*(6), 1–13. https://doi.org/10.3390/foods9060772

Zhang, J. Y., Pandya, J. K., McClements, D. J., Lu, J., & Kinchla, A. J. (2022). Advancements in 3D food printing: a comprehensive overview of properties and opportunities. *Critical Reviews in Food Science and Nutrition, 62*(17), 4752–4768. https://doi.org/10.1080/10408398.2021.1878103

Zhu, S., Stieger, M. A., van der Goot, A. J., & Schutyser, M. A. I. (2019). Extrusion-based 3D printing of food pastes: Correlating rheological properties with printing behaviour. *Innovative Food Science and Emerging Technologies, 58*. https://doi.org/10.1016/j.ifset.2019.102214